

# Assessing the performance of MoTe<sub>2</sub> based solar cell with Cu<sub>2</sub>O hole transport layer through device simulation

Naimur Rahman<sup>1</sup> · Md. Dulal Haque<sup>2,3</sup> · Md. Ferdous Rahman<sup>4</sup> · Md. Mominul Islam<sup>1</sup> · Most. Airin Nahar Juthi<sup>1</sup> · Anita Rani Roy<sup>1</sup> · Most. Alema Akter<sup>1</sup> · Md. Foridul Islam<sup>1</sup>

Received: 15 July 2023 / Accepted: 1 September 2023

Published online: 13 September 2023

© The Author(s) 2023 [OPEN](#)

## Abstract

In this study, the SCAPS-1D tool has been used to numerically examine the performance of Transition Metal Dichalcogenides (TMDC) based Molybdenum ditelluride (MoTe<sub>2</sub>) solar cells containing CdS electron transport layer (ETL) and Cu<sub>2</sub>O hole transport layer (HTL). Based on the photovoltaic cell parameters, including absorber layer thickness, temperature, defect density, the effects of series and shunt resistance, and electron affinity, the structure of both MoTe<sub>2</sub> based solar cells with and without the usage of the HTL has been analyzed. With 1.1 μm thickness of MoTe<sub>2</sub> and doping density of  $5 \times 10^{15} \text{ cm}^{-3}$ , Al/FTO/CdS/MoTe<sub>2</sub>/Cu<sub>2</sub>O/Ni heterojunction's solar cell proposed structure has been optimized. The final power conversion efficiency (PCE) = 32.38%, open-circuit voltage ( $V_{oc}$ ) = 1.07 V, short-circuit current ( $J_{sc}$ ) = 35.12 mA/cm<sup>2</sup>, and fill factor (FF) = 86.32% has been determined from the optimized structure. The determined results indicate a suitable path for the realization of low cost and high efficiency MoTe<sub>2</sub>-based solar cell.

**Keywords** Transition metal dichalcogenides · Thin-film solar cell · SCAPS · Hole transport layer · MoTe<sub>2</sub>

## 1 Introduction

Solar cells are the devices for harvesting electricity from photon energy. The vast range of usages of solar cells demonstrates its potential as an ultimate source of clean energy for mankind. The first-generation crystalline silicon (c-Si) solar cells have dominated the PV market, accounting for 95% of global market share, while thin-film PV technologies, such as CdTe, Cu(In,Ga)Se<sub>2</sub> (CIGS), and thin-film Si, make up the remaining 5% [1]. The highest conversion efficiency achieved to date for c-Si-based solar cells is 26.7% [2]. But their cost and the challenges of thick and expensive Si wafers, high processing temperatures, high-vacuum fabrication processes, and other complex and costly processing technologies limit their scalability.

**Supplementary Information** The online version contains supplementary material available at <https://doi.org/10.1007/s43939-023-00061-7>.

✉ Md. Dulal Haque, [dhaque@hstu.ac.bd](mailto:dhaque@hstu.ac.bd); Naimur Rahman, [naimurrahman8105@gmail.com](mailto:naimurrahman8105@gmail.com); Md. Ferdous Rahman, [ferdousapee@gmail.com](mailto:ferdousapee@gmail.com); Md. Mominul Islam, [momin.phy@tch.hstu.ac.bd](mailto:momin.phy@tch.hstu.ac.bd); Most. Airin Nahar Juthi, [airinjuthi@gmail.com](mailto:airinjuthi@gmail.com); Anita Rani Roy, [anianitaray@gmail.com](mailto:anianitaray@gmail.com); Most. Alema Akter, [apifb90@gmail.com](mailto:apifb90@gmail.com); Md. Foridul Islam, [connect.foridul@gmail.com](mailto:connect.foridul@gmail.com) | <sup>1</sup>Department of Physics, Hajee Mohammad Danesh Science and Technology University, Dinajpur 5200, Bangladesh. <sup>2</sup>Department of Electronics and Communication Engineering, Hajee Mohammad Danesh Science and Technology University, Dinajpur 5200, Bangladesh. <sup>3</sup>State Key Laboratory of Infrared Physics, Shanghai Institute of Technical Physics, Chinese Academy of Sciences, 188 Xinlai Rd, Jiading District, Shanghai 201800, China. <sup>4</sup>Advanced Energy Materials and Solar Cell Research Laboratory, Department of Electrical and Electronic Engineering, Begum Rokeya University, Rangpur 5400, Bangladesh.



To address these challenges, researchers are exploring new materials and production mechanisms to increase the efficiency and reduce the cost of solar cells. Among the many thin-film solar cell (TFSC) technologies that have emerged, only a few, such as CdTe, CIGS, and perovskite solar cells, have achieved commercial success due to their high efficiency. Copper zinc tin sulfide (CZTS), an earth-abundant solar cell material, has emerged as a promising replacement for CIGS, with a theoretical efficiency of 30.79% [3, 4]. However, the use of toxic and rare earth materials in CdTe solar cells, material or resource constraints, and the complicated fabrication process of CIGS technology are limiting factors for their industrial scalability [5, 6]. To overcome these challenges, researchers have turned to TMDCs, which are non-toxic, low-cost, earth-abundant materials. TMDCs offer several advantages as PV absorbers, including suitable bandgap, high absorption coefficients, high carrier transportation, and mechanical flexibility [7–9]. In particular, monolayer TMDC compounds, such as  $\text{MX}_2$  (where M is a transition metal atom, such as Mo, W, Nb, Ti, and X is a chalcogen atom, such as S, Se, Te), have gained popularity for their use in PV cells [10, 11].

The  $\text{MoTe}_2$  is an emerging absorber material known for its stability, non-toxicity, and cost effectiveness [12]. Mechanical exfoliation combined with 2 H-MoSe<sub>2</sub> can produce few-layered 2 H-MoTe<sub>2</sub> crystals which have the characteristic of Van der Waals planes with low surface defect densities [13, 14].  $\text{MoTe}_2$  has attracted great attention as a light absorbing material having good properties such as excellent optical absorption coefficient around  $10^5 \text{ cm}^{-1}$ , tunable band gap of around 1.2 eV, high carrier mobility, non-toxicity, and earth abundant for low cost TFSCs structures [15–17]. Due to these promising properties, several PV cell structures of  $\text{MoTe}_2$ -based solar cells have been constructed and analyzed experimentally and analytically in earlier research to attain better performance [12, 18, 19]. Dye-sensitized solar cell constructed using a photocathode made from  $\text{MoTe}_2$  atomic layers shows a high PCE of 8.44% [19]. The optimized  $\text{MoTe}_2$  conversion efficiency (CE) revealed a power conversion efficiency (PCE) of 7.25% under a simulated solar illumination of  $100 \text{ mW cm}^{-2}$  (AM 1.5) [20]. The use of  $\text{MoTe}_2$  as an absorber layer in thin-film solar cells has not yet been experimentally explored. However, several research groups have investigated the photovoltaic properties of  $\text{MoTe}_2$ -based solar cells numerically. In one study,  $\text{SnO}_2/\text{Zn}_2\text{SnO}_2/\text{CdS}/\text{MoTe}_2/\text{ZnTe}$  heterojunction solar cells with a  $\text{MoTe}_2$  thickness of  $1 \mu\text{m}$  were found to have a PCE of 25.16% [21]. A similar structure has been studied but substituted  $\text{As}_2\text{Te}_3$  for ZnTe and achieved a PCE of 25.06% [22]. In another research, the use of CZT instead of ZnTe obtained a PCE of 25.11% with a slightly thinner  $\text{MoTe}_2$  layer ( $0.8 \mu\text{m}$ ) [12]. The theoretical maximum efficiency of optimized FTO/CdS/ $\text{MoTe}_2$ / $\text{Cu}_2\text{Te}$  photovoltaic cell has been observed as 29.13% [15]. These results suggest that  $\text{MoTe}_2$ -based solar cells have significant potential for high-performance photovoltaic applications.

The performance parameters of  $\text{MoTe}_2$  solar cell (SC), including  $V_{\text{OC}}$ ,  $J_{\text{SC}}$ , FF, and PCE, have not been achieved at an expected level compared to other heterojunction TFSCs [2]. The carrier recombination at the junction reduces  $V_{\text{OC}}$  and  $J_{\text{SC}}$ , and the absence of a back surface field (BSF) or hole transport layer (HTL) and buffer layer causes inadequate carrier transportation, accumulation at the electrodes, and carrier recombination at the junction, leading to a reduction in  $V_{\text{OC}}$  and  $J_{\text{SC}}$  and degradation of conversion efficiency [23, 24]. Interface recombination loss results in a poor value of  $V_{\text{OC}}$  and  $J_{\text{SC}}$ , and reported HTLs are not efficient for transportation and collection of carriers, resulting in deficits in the performance parameters. To address these issues, redesigning  $\text{MoTe}_2$  solar cells with an efficient and cost-effective HTL layer is crucial. The incorporation of p-type HTL enables hole transportation easier from absorber layer to the back metallic contact due to low valence band offset [25, 26]. It boosts the carrier collecting efficiency and reduce the rate of recombination at the back-contact surface [27].

HTLs come in variety of forms, e.g., organic, small molecule-based, and inorganic ones. Conjugated polymers, which have good film-forming capabilities and high hole mobility, are the building blocks of organic HTLs. poly(3,4-ethylenedioxythiophene):poly(styrenesulfonate) (PEDOT:PSS) and poly(3-hexylthiophene) (P3HT) are two examples of frequently used polymer-based HTLs. These HTLs are popular for their ease of processing and incorporation into organic PV devices [28, 29]. Small molecule-based HTLs are made of small organic molecules. Some commonly used small molecule-based HTLs include copper phthalocyanine (CuPc) and 2,9-dimethyl-4,7-diphenyl-1,10-phenanthroline (BCP). Because they are simple to deposit on a variety of substrates and have good thermal stability, these HTLs are popular [30, 31]. Inorganic HTLs are made of inorganic materials such as metal oxides and chalcogenides. Some commonly used inorganic HTLs include  $\text{SnO}_2$ ,  $\text{TiO}_x$ ,  $\text{NiO}_2$ ,  $\text{MoO}_x$ ,  $\text{V}_2\text{O}_5$ , ZnO,  $\text{Cu}_2\text{O}$ , CuSCN, and  $\text{WO}_x$ . Due to their great hole mobility and exceptional stability under ambient circumstances, these HTLs are appreciated. Among them,  $\text{Cu}_2\text{O}$  is considered a promising material for use as an HTL layer due to its high hole mobility and excellent electrical properties. With a cubic structure and a lattice constant of  $4.2696 \text{ \AA}$ ,  $\text{Cu}_2\text{O}$  is composed of copper atoms in the fcc sublattice and oxygen atoms in the bcc sublattice [32]. As a p-type semiconductor, it has unique physical characteristics e.g., high carrier mobility greater than  $100 \text{ cm}^2/(\text{V}\cdot\text{s})$  and long carrier diffusion length [33]. Nitrogen-doped  $\text{Cu}_2\text{O}$  was first reported to be used as an HTL in 2013, showing sizeable enhancements in fill-factor and PCE [34]. It was observed that the utilization of  $\text{Cu}_2\text{O}$  as a HTL provides protection against moisture, thereby enhancing the cell's resistance to degradation [35]. The unique characteristics of  $\text{Cu}_2\text{O}$  make it a promising candidate for HTL material.

This research investigates the PV performance parameters of the proposed (Al/FTO/CdS/MoTe<sub>2</sub>/Cu<sub>2</sub>O/Ni) MoTe<sub>2</sub>-based thin-film heterojunction SC with and without HTL. The investigation of the influence of the thickness, carrier concentration, defect density, working temperature, band alignment, electron affinity, back surface recombination velocity, series and shunt resistance on SC output parameters has been analyzed for the baseline (without HTL) and the proposed (with HTL) structure. The SCAPS-1D simulator has been used to optimize the device structure and achieve better photoconversion efficiency in a cost-effective manner.

## 2 Design and characteristics of the device

Figure 1a illustrates the proposed FTO/CdS/MoTe<sub>2</sub>/Cu<sub>2</sub>O SC structure. Transparent conducting fluorine doped tin oxide (FTO) has been used as the window layer due to its excellent thermal stability and transparency. Large optical throughput is provided by the broad band gaps of FTO and CdS in hetero-junction structures. The CdS ETL can create a suitable junction with MoTe<sub>2</sub> due to its favorable electron affinity. In the SC structure shown in Fig. 1a, the Cu<sub>2</sub>O HTL with an appropriate band gap and electron affinity aids in forming a correct hetero-junction between the p-MoTe<sub>2</sub> absorber and p<sup>+</sup>-Cu<sub>2</sub>O. The Al and Ni are employed for the front and rear contact, respectively. Figure 1b illustrates the energy band diagram of the FTO/CdS/MoTe<sub>2</sub>/Cu<sub>2</sub>O structure.

Since the Cu<sub>2</sub>O layer's valence band is located at a lower energy level than the MoTe<sub>2</sub> layer, a bigger conduction band offset (CBO) is produced. The bigger CBO blocks the movement of electrons from the MoTe<sub>2</sub> absorption layer to the Ni-containing back metal. As a result, the loss due to interface recombination is reduced. Because of the extremely low valance band offset (VBO) between MoTe<sub>2</sub> and Cu<sub>2</sub>O (0.02 eV), holes can be moved from the p-MoTe<sub>2</sub> to the rear metal contact using p<sup>+</sup>-Cu<sub>2</sub>O. Since that the CBO between CdS and MoTe<sub>2</sub> is just 0.1 eV, the produced photoelectrons inside the p-MoTe<sub>2</sub> absorber can travel effortlessly via the n-CdS ETL to FTO. Yet, with large VBO of 1.3 eV, it prevents the movement of holes. Since CdS has a wider band gap than the p-MoTe<sub>2</sub> absorber layer (2.45 eV), more electron-hole pairs can be generated through photon absorption [36, 37].

The One-dimensional Solar Cell Capacitance Simulator (SCAPS-1D) application has been utilized for the simulation of the device. Marc Burgelman et al., of the University of Ghent in Belgium created the promising software SCAPS-1D. By resolving basic equations like the continuity equation in steady-state situations, it may be utilized to anticipate as well as analyze the optoelectronic properties of solar cell structures [38]. Quantum efficiency (QE) and J-V characteristics are assessed at a specific working environment using this numerical method for evaluating energy bands, carrier generation and recombination rate, and quantum efficiency. Furthermore, the impact of variation of thickness, doping concentration, each layer's defect concentration, the junction's defect density, working temperature, and surface recombination velocity (SRV) on performance has been examined. The simulations were run using a radiation setting 1000 W/m<sup>2</sup>, air mass

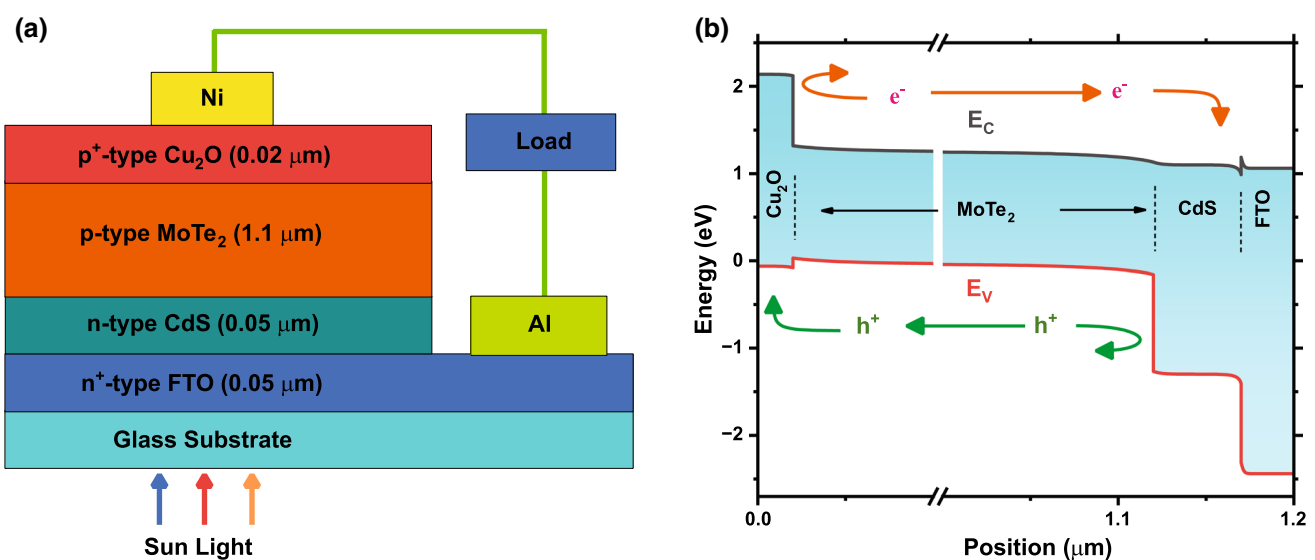


Fig. 1 Design of Al/FTO/CdS/MoTe<sub>2</sub>/Cu<sub>2</sub>O/Ni solar cell **a** schematic structure and **b** energy band diagram

**Table 1** Device parameters used in the simulation [39–42]

Parameters (unit)	FTO	CdS	MoTe <sub>2</sub>	Cu <sub>2</sub> O
Thickness (μm)	0.05	0.05	0.001–6.0	0.02*
E <sub>g</sub> (eV)	3.5	2.4	1.29	2.2
χ (eV)	4.0	4.2	4.2	3.0–3.8
ε <sub>r</sub> (eV)	9.0	10.0	13.0	7.5
N <sub>c</sub> (cm <sup>-3</sup> )	1 × 10 <sup>19</sup>	2.2 × 10 <sup>18</sup>	3 × 10 <sup>18</sup>	2 × 10 <sup>19</sup>
N <sub>v</sub> (cm <sup>-3</sup> )	1 × 10 <sup>19</sup>	1.8 × 10 <sup>19</sup>	4 × 10 <sup>16</sup>	1 × 10 <sup>19</sup>
μ <sub>e</sub> (cm <sup>2</sup> /V.s)	100	100	110	200
μ <sub>h</sub> (cm <sup>2</sup> /V.s)	25	25	426	8600
ND (cm <sup>-3</sup> )	2 × 10 <sup>19</sup>	1 × 10 <sup>18</sup>	0	0
NA (cm <sup>-3</sup> )	0	0	1 × 10 <sup>12</sup> – 1 × 10 <sup>21</sup>	1 × 10 <sup>18</sup>
Defect type	Single-Acceptor	Single-Acceptor	Single-Donor	Single-Donor
Energy distribution	–	Gaussian	Gaussian	Gaussian
Defect density N <sub>t</sub> (cm <sup>-3</sup> )	1 × 10 <sup>14</sup>	1 × 10 <sup>14</sup>	1 × 10 <sup>12</sup> – 1 × 10 <sup>20</sup>	1 × 10 <sup>15</sup>

**Table 2** Interface defect parameters

Parameters (unit)	CdS/MoTe <sub>2</sub> interface	MoTe <sub>2</sub> /Cu <sub>2</sub> O interface
Defect type (μm)	Neutral	Neutral
o <sub>e</sub> (cm <sup>-2</sup> )	1 × 10 <sup>-19</sup>	1 × 10 <sup>-19</sup>
o <sub>h</sub> (cm <sup>-2</sup> )	1 × 10 <sup>-19</sup>	1 × 10 <sup>-19</sup>
E <sub>t</sub> (eV)	above the highest E <sub>v</sub>	above the highest E <sub>v</sub>
E <sub>r</sub> (eV)	0.60	0.60
Total defect density (cm <sup>-2</sup> )	1 × 10 <sup>10</sup> – 1 × 10 <sup>21</sup>	1 × 10 <sup>10</sup> – 1 × 10 <sup>21</sup>

spectrum of 1.5G and operating temperature of 300 K. Table 1 provides a summary of the material and Table 2 lists the interface defect parameters for CdS/MoTe<sub>2</sub> and MoTe<sub>2</sub>/Cu<sub>2</sub>O interface.

### 3 Results and discussion

#### 3.1 Impact of the absorber layer thickness

The efficiency of thin-film photovoltaic cells greatly depends on the thickness and carrier concentration of the absorber layer. These two factors play a crucial role in determining the rates of photocarrier generation and extraction. An increase in the thickness of the absorber layer leads to an increase in carrier generation and recombination rates. It is worth noting that controlling the thickness and carrier concentration of the absorber layer can significantly enhance the efficiency of the thin-film PV cells. Therefore, optimizing these factors is essential in achieving high-performance photovoltaic devices. In order to analyze the effects of these parameters on the photovoltaic performance parameters of the cells designed in this study, the parameters of the other layers were held constant. Figure 2a shows how the variation of MoTe<sub>2</sub> thickness affects the PV parameters of V<sub>oc</sub>, J<sub>sc</sub>, FF and PCE for proposed and baseline SC. To test the impact on the PV parameters, the MoTe<sub>2</sub> layer thickness was varied from 0.001 to 6 μm. The J<sub>sc</sub> increases rapidly from 1.51 to 34.63 mA/cm<sup>2</sup> for thickness values of 0.001–1 μm, suggesting that the increase in thickness has boosted absorption. However, if the absorber layer is too thick, the distance that minority charge carriers can travel without recombining is shorter than the thickness of the layer. This leads to a higher rate of recombination, causing J<sub>sc</sub> to become roughly constant above this thickness. This has caused the J<sub>sc</sub> to be roughly constant at 35 mA/cm<sup>2</sup> for the thickness after 1 μm. In the case of FF, a marginal reduction from 85.09 to 84.87% for 0.1–0.3 μm thickness was observed, followed by a steady increase for the proposed SC. For the baseline SC, FF increased from 85.88 to 86.62% for a brief thickness range of 0.001–0.2 μm. After that, it reduced quickly at 0.3–0.7 μm, giving a minimum of 84.51%, indicating that recombination loss is dominant in this thickness region. From 0.7 μm, FF increased at a similar rate to that of with the baseline structure. Without the HTL layer, poor charge extraction and high recombination losses, led to a low FF for absorber layers thinner than 0.2 μm. The Cu<sub>2</sub>O HTL layer improves

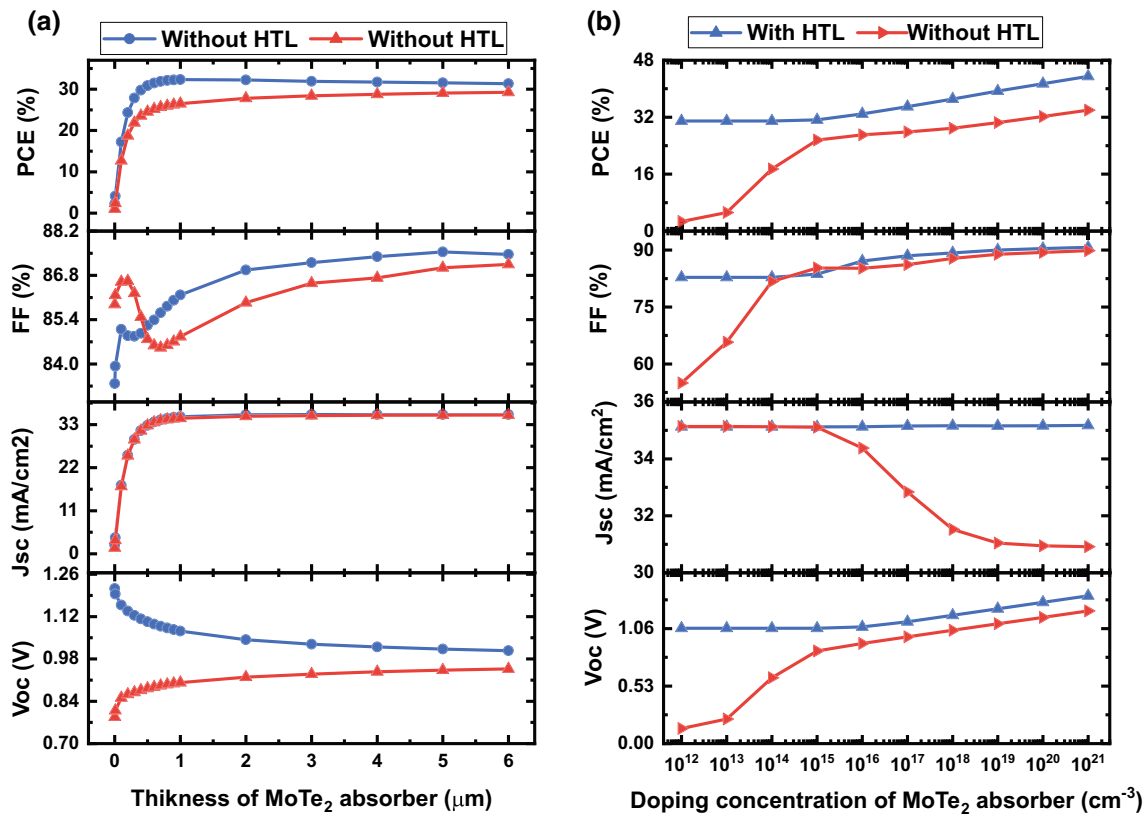


Fig. 2 Variation of PV parameters due to change of **a** thickness and **b** doping concentration

charge transport and reduce recombination losses at the interface between the absorber layer and the electrode. Consequently, the FF initially dropped slightly (85.09–84.87%) as the absorber layer thickness increased from 0.1 to 0.3 μm. This drop occurs because the improved charge transport leads to more effective charge extraction. However, as the absorber layer thickness continued to increase, the losses due to charge carrier recombination became more significant, and FF started to increase steadily. Beyond 0.2 μm, for the proposed SC, the charge transport properties were improved, leading to an increase in FF. This phenomenon is influenced by several factors. According to a study by Meng et al. [43], increasing the thickness of the absorber layer can improve the FF of the solar cell, even though it also increases the series resistance. The reason is that thicker MoTe<sub>2</sub> layers have better light absorption and carrier collection efficiency, which can compensate for the loss of voltage due to series resistance. Other studies suggest that the increase in series resistance is offset by increase in shunt resistance, which enhance carrier transport and reduce the recombination losses [44, 45].

In the absence of HTL, V<sub>oc</sub> increased gradually from 0.79 to 0.90 V for thickness range of 0.001–1 μm, while in the presence of HTL, V<sub>oc</sub> decreased gradually from 1.21 to 1.07 V. Cu<sub>2</sub>O/MoTe<sub>2</sub> interface creates a strong electric field which is the cause for the initial high V<sub>oc</sub>. Beyond this thickness, V<sub>oc</sub> remained around 0.94 V for baseline structure and 1.1 V for the proposed structure. All of the aforementioned study demonstrates that utilizing HTL has a positive impact on the solar cell's performance and efficiency because it increases carrier collection efficiency by improving the absorption of lower photon energies by reducing the rate of back surface recombination. The device's J<sub>sc</sub> and PCE values were not changed after 1.1 μm. As a result, it is regarded as having a 1.1 μm optimum thickness to achieve best performance. 1.07 V and 35.12 mA/cm<sup>2</sup> are the optimal value of V<sub>oc</sub> and J<sub>sc</sub> respectively at 1.1 μm MoTe<sub>2</sub> thickness. Based on the obtained results, it can be inferred that for the proposed structure, the values of J<sub>sc</sub> and PCE increase with rising MoTe<sub>2</sub> thickness, while the value of V<sub>oc</sub> increases with decreasing absorber thickness which inclines with previous results [42, 46].

### 3.2 Effect of absorber doping concentration

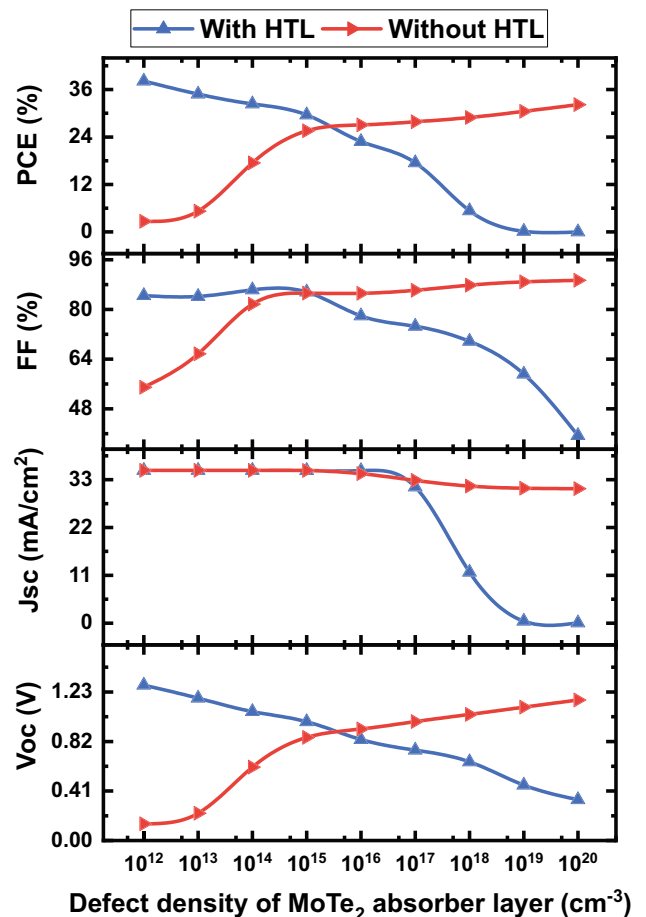
Proper doping can improve the collection efficiency of the generated carriers and enhance the V<sub>oc</sub>, J<sub>sc</sub> and FF of the solar cell. However, excessive doping can also introduce defects and trap states, which can increase the recombination losses

and degrade the performance. Therefore, optimizing the doping concentration is necessary for achieving the maximum efficiency of a solar cell. Keeping all other variables unchanged, the MoTe<sub>2</sub> absorber layer's doping concentration range was expanded from  $1 \times 10^{12}$  to  $1 \times 10^{21}$  cm<sup>-3</sup>. The impact of the doping density in the MoTe<sub>2</sub> absorber layer on  $V_{oc}$ ,  $J_{sc}$ , FF, and PCE is shown in Fig. 2b.  $V_{oc}$  is observed to be nearly constant (1.06 V) in the case of the proposed SC from  $1 \times 10^{12}$  to  $1 \times 10^{16}$  cm<sup>-3</sup>, after which it steadily increased, giving a maximum  $V_{oc}$  of 1.36 V for  $1 \times 10^{21}$  cm<sup>-3</sup> doping density. For the baseline structure, a steep increase was observed in  $V_{oc}$  (0.14–0.85 V) for the range  $1 \times 10^{12}$  to  $1 \times 10^{15}$  cm<sup>-3</sup> and then a gradual scaling, thereafter, peaking at 1.22 V. The formation of a well-defined Cu<sub>2</sub>O/MoTe<sub>2</sub> interface results in a lower density of surface states and reduced recombination of charge carriers. In the absence of the HTL,  $J_{sc}$  was roughly constant (35.11 mA/cm<sup>2</sup>) up to  $1 \times 10^{15}$  cm<sup>-3</sup> before decreasing to the lowest value (30.91 mA/cm<sup>2</sup>) for the highest concentration of  $1 \times 10^{21}$  cm<sup>-3</sup>. The change in  $J_{sc}$  in the proposed structure was minimal. It is a straight horizontal line of 35.15 mA/cm<sup>2</sup>. In this structure, FF and PCE maintained a constant value of 83.67% and 31.24% respectively, up to  $5 \times 10^{15}$  cm<sup>-3</sup>. For the baseline device the increase is rather abrupt. Both gradually grow afterwards. The highest FF and PCE for the proposed structure for doping density of  $1 \times 10^{21}$  cm<sup>-3</sup> is 89.82% and 43.48% respectively. The interface and bulk recombination rates may enhance due to the increasing free carrier density. The doping concentration of  $5 \times 10^{15}$  cm<sup>-3</sup> is regarded as the ideal value in this study to attain optimal device efficiency of developed structure which is lower than previous studies [15, 22].

### 3.3 Effect of variation of defect density of the absorber

In terms of a single donor, we have studied bulk defect density in the range of  $1 \times 10^{12}$  to  $1 \times 10^{20}$  cm<sup>-3</sup>. The variations in cell output for the defect density in the absorber layer with and without the HTL layer are shown in Fig. 3. The curves for all PV parameters show downwards trend for the proposed device. For increasing the defect density from  $1 \times 10^{12}$  to  $1 \times 10^{20}$  cm<sup>-3</sup>,  $V_{oc}$ , FF and PCE dropped from 1.29 to 0.34 V, 84.47 to 39.44%, 38.15 to 0.0056% respectively. In the case of  $J_{sc}$  it remained constant (35.12 mA/cm<sup>2</sup>) up to  $1 \times 10^{16}$  cm<sup>-3</sup>, then decreased quickly to zero. In the baseline structure, the

**Fig. 3** The impact of absorber defect density on PV parameters



reverse order of change was observed where  $V_{oc}$ , FF and PCE increased from 0.14 to 1.16 V, 54.98 to 89.38%, 2.68 to 32.20% respectively. The values of these parameters became identical to each structure at defect density around  $1 \times 10^{15} \text{ cm}^{-3}$  ( $V_{oc} = 0.87 \text{ V}$ , FF = 85.28%, and PCE = 27.57%).  $J_{sc}$  maintained a constant value of  $35.12 \text{ mA/cm}^2$  up to  $1 \times 10^{16} \text{ cm}^{-3}$  for both structures and thereafter did not decrease much in the baseline structure.

In the absence of  $\text{Cu}_2\text{O}$  HTL, the PV parameters benefit from the defect density of  $\text{MoTe}_2$  absorber due to improved charge collections and improved absorption of photons. However, the decreasing  $J_{sc}$  indicates that, recombination loss becomes dominant and cancels out these improvements. The proposed HTL model does not require densely defected  $\text{MoTe}_2$  absorber to yield better performance. The performance of a solar cell is significantly impacted by defects in bulk material [47]. More defects in the absorption layer led to higher non-radiative recombination of free carriers of SC, which lowers the solar cell's overall efficiency characteristics [48]. From an experimental standpoint, the absorber material contains several defects, including surface defects, secondary phases, and structural defects [49]. To produce improved PCE, it is crucial to maintain a low defect concentration in the  $\text{MoTe}_2$  layer. For the purposes of this study, we maintained the defect concentration at  $1 \times 10^{14} \text{ cm}^{-3}$  in order to optimize the PCE of the designed structure.

### 3.4 Effect of electron affinity of the HTL

The electron affinity of the HTL in a solar cell is a critical parameter that affects the energy level alignment between the HTL and the adjacent layers, such as the active layer and the ETL. The electron affinity determines the potential barrier that the electrons must overcome when moving from the active layer to the HTL. Additionally, it controls the quality of the junction contact [50]. In an ideal solar cell, the electron affinity of the HTL should be higher than that of the active layer. This condition ensures that the electrons will flow smoothly from the active layer to the HTL, thereby minimizing the recombination losses at the interface. Additionally, the electron affinity of the HTL should be lower than that of the ETL, so that the holes can easily move from the HTL to the ETL and then to the electrode. The effect of the electron affinity of the HTL with values ranging from 3.0 to 3.8 eV has been examined on the electric field and current densities in the context of the performance of solar cells, as demonstrated in Fig. 4a–d and in Fig. 5a, b. The results indicate that the electron affinity of the  $\text{Cu}_2\text{O}$  HTL significantly impacts the SCs' performance.

In Fig. 4a, the J-V curve for different electron affinities is depicted. The J-V curve starts at  $J = 35.08 \text{ mA/cm}^2$  and  $V = 0 \text{ V}$ . The maximum voltage found before null current density is 1.06 V, which holds true for the values 3.2–3.8 eV. While studying the effect of HTL thickness on the electric field for different values of electron affinity, we observed that at the thickness value of  $0.02 \mu\text{m}$ , the electric field has distinct peaks on both positive and negative sides,  $3.7 \times 10^5$  and  $-2.8 \times 10^5 \text{ V/cm}$  respectively. The formation of p<sup>+</sup>-p junctions in the  $\text{MoTe}_2/\text{Cu}_2\text{O}$  interface generates high electric field. The impact of electron affinity on the interface recombination current density is presented in Fig. 4c. The interface recombination as well as SRH recombination decrease for higher values of electron affinity. At the lowest value of electron affinity (3 eV), the maximum value of interface recombination current was  $40.47 \text{ mA/cm}^2$ , while it was only  $2.36 \times 10^{-4} \text{ mA/cm}^2$  at the electron affinity of 3.8 eV for 1 V. As seen in Fig. 4d, the SRH recombination current did not vary significantly with the change of electron affinity, remaining around  $45 \text{ mA/cm}^2$  at a voltage of 1.08 V. A higher electron affinity value reduces the interface barrier potential and enables an increase in carrier flow at the  $\text{MoTe}_2/\text{Cu}_2\text{O}$  interface, contributing to a decrease in the interface and SRH recombination current, as previously reported [51, 52]. From Fig. 5a, it is evident that,  $V_{oc}$  increased from 0.99 to 1.06 V for 3.0 to 3.2 eV electron affinity and kept this value till 3.8 eV. The variation in energy band alignment due to fluctuations in electron affinity is presented in Fig. 5(a). According to the simulation results, the device performance deteriorates when electron affinity is too high or too low, owing to

the disparity in  $E_v$  levels between the HTL and  $\text{MoTe}_2$ . An increase in electron affinity value reduces the barrier height at the  $\text{MoTe}_2/\text{Cu}_2\text{O}$  interface, which improves the hole transportation through the junction. The PV performance with respect to electron affinity presented in Fig. 5b demonstrates the overall effectivity of electron affinity value.  $V_{oc}$ ,  $J_{sc}$ , FF and PCE for 3 eV electron affinity were 0.99 V,  $35.08 \text{ mA/cm}^2$ , 83.57%, and 28.93%, respectively.  $V_{oc}$  and  $J_{sc}$  improved thereafter and maintained a constant value of 1.07 V and  $35.13 \text{ mA/cm}^2$ , respectively. Additionally, FF and PCE improved and maintained constant values (FF = 86.32%, PCE = 32.38%) but declined after 3.6 eV. The region of flat band energy can be identified by the efficiency stepping down in the suggested SC below the electron affinity value of 3.2 eV and above 3.6 eV. If the VBO between HTL and the absorber layer is low, the performance of the SC is superior in comparison to higher VBO values. A low electron affinity leads to a high VBO between  $\text{MoTe}_2$  and  $\text{Cu}_2\text{O}$ , resulting in an increased possibility of charge carrier recombination that reduces the PV parameters of the proposed heterojunction solar cell structure, as illustrated in Fig. 5b [53]. To achieve the highest PCE, we suggest an optimal electron affinity of 3.4 eV for  $\text{Cu}_2\text{O}$ .

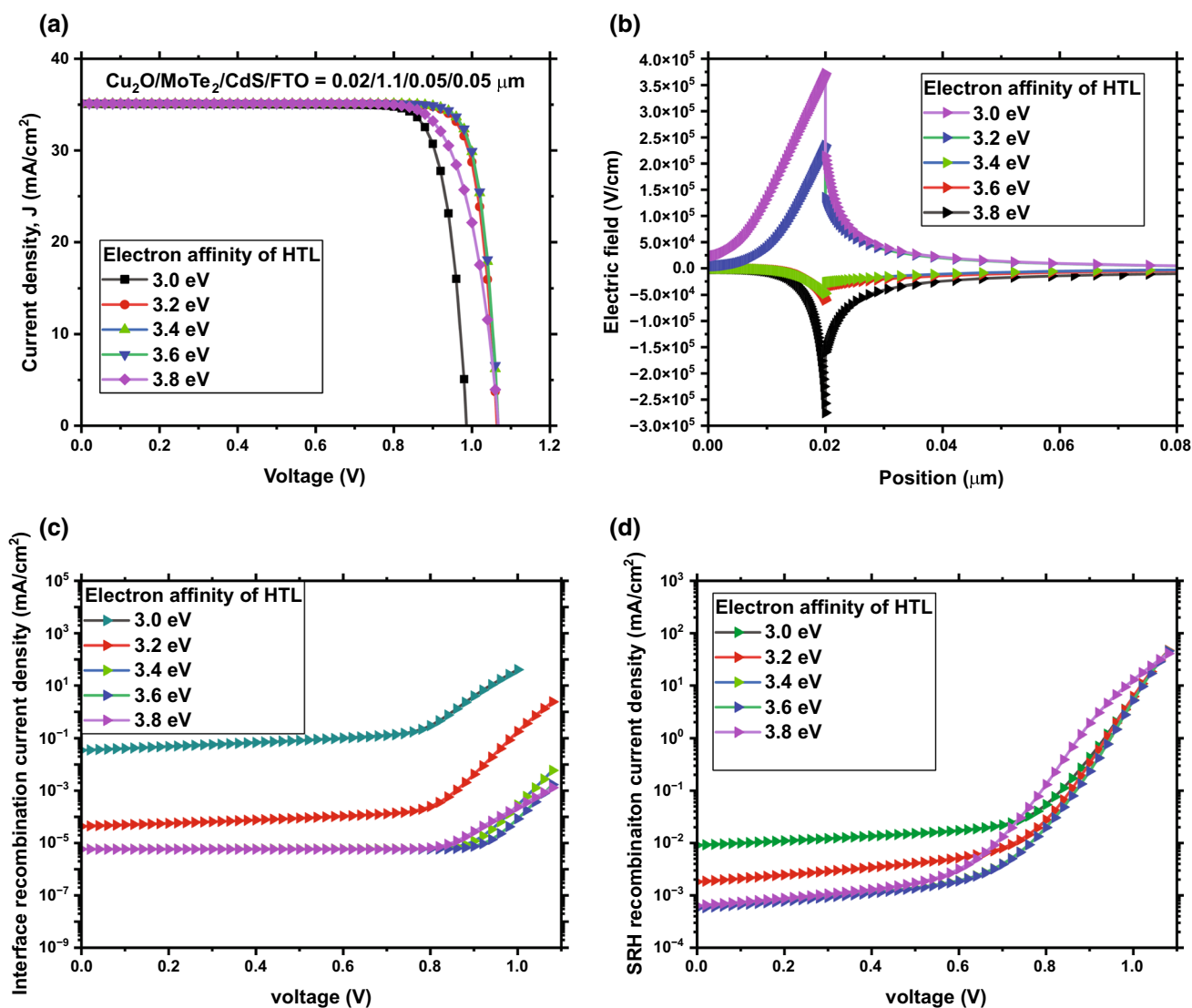


Fig. 4 The effect of electron affinity of HTL layer on PV parameters **a** J-V curve, **b** electric field, **c** Interface recombination and **d** SRH recombination

### 3.5 Effect of contact work function on PV performance

Establishing an ohmic contact will ensure proper electron collection from the PV devices. The ideal metal work function for the front contact metal was determined through simulation, leading to the choice of Al for this investigation. The front contact’s work function was incrementally varied from 3.9 eV to 4.7 eV. Based on  $V_{oc}$ ,  $J_{sc}$ , FF and PCE, the performance of the cells was evaluated as shown in Fig. 6a. It is noteworthy that  $V_{oc}$  (1.07 V) and  $J_{sc}$  (35.11 mA/cm<sup>2</sup>) remained constant up to 4.6 eV. Similarly, PCE (32.37%) was stable up to 4.5 eV, whereas the FF (86.32%) remained steady up to 4.4 eV and then rapidly degraded. The decline in performance can be attributed to the emergence of a barrier arising from the work function of the front contact/ETL interface, which is influenced by a high-value work function [54]. These results led to the conclusion that front contact metal with a work function lower than 4.4 eV is suitable for optimal device performance.

To extend our analysis, we investigated the effect of back contact work function variations, ranging from 4.5 eV to 6.0 eV. From Fig. 6b, it was observed that work function of around 5.0 eV is sufficient to achieve maximum performance parameters ( $V_{oc} = 1.07$  V,  $J_{sc} = 35.12$  mA/cm<sup>2</sup>, FF = 79%, PCE = 29.6%) for the proposed structure. However, for the baseline structure, additional 0.5 eV of work function is required to achieve the same output. The reason for this difference is that Cu<sub>2</sub>O HTL affects the energy band alignment between MoTe<sub>2</sub> and the back contact. This band alignment facilitates the



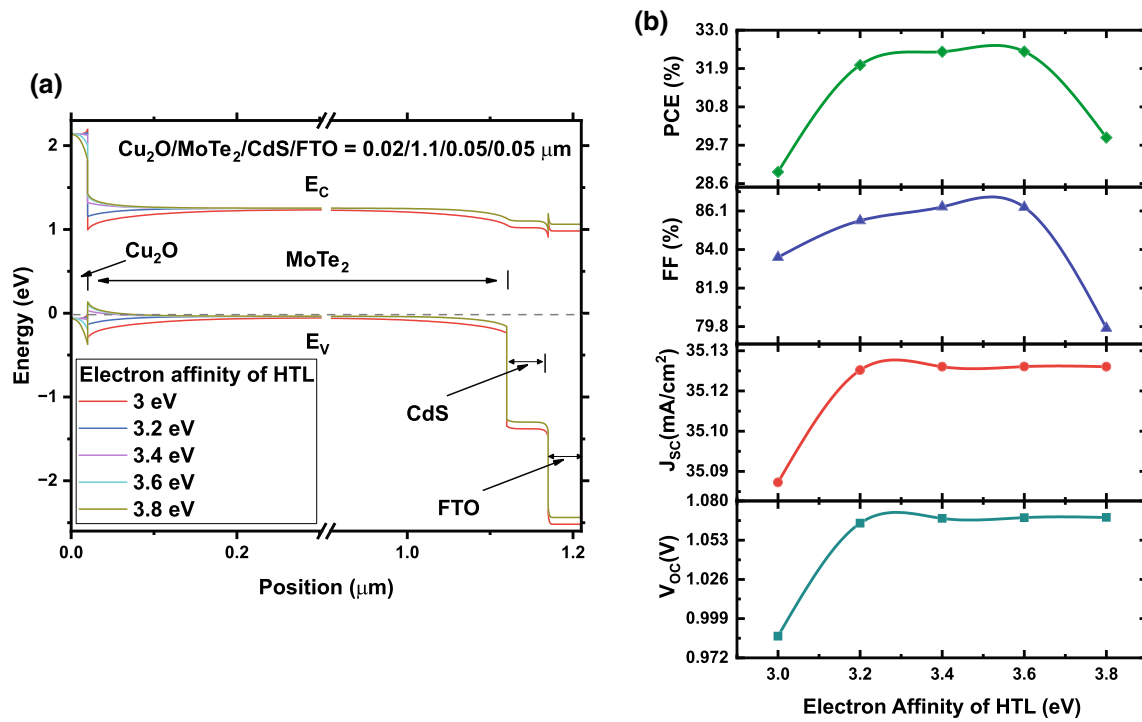


Fig. 5 The effect of electron affinity of HTL layer on **a** energy diagram, **b** PV parameters

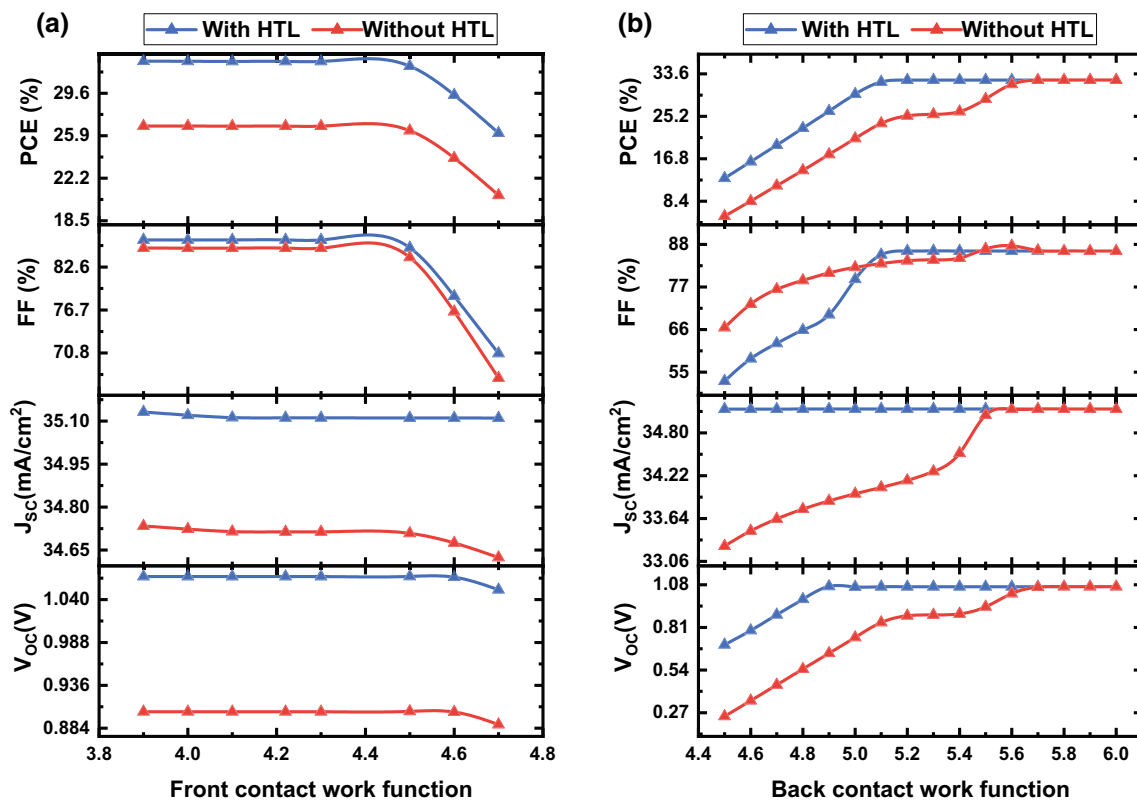


Fig. 6 The variation of PV output parameters with varying work function of **a** front contact and **b** back contact

separation and transport of charge carriers across the interface. Consequently, a lower work function of back contact is required to achieve maximum performance. A work function of 5.42 eV for Ni was considered as a suitable back contact for this device [55].

### 3.6 Effect of interface defect density

Photogenerated carriers, i.e. electrons and holes, are created at the interface of the absorber layer and the transport layer. These carriers then move towards the electrodes and contribute to the current. However, defects at the interface can trap these carriers, preventing them from contributing to the current. These defects can also cause recombination, where electrons and holes combine and release their energy as heat, without contributing to the current. Non-radiative recombination channels caused by interface defects can therefore reduce the efficiency of the solar cell by reducing the number of photogenerated carriers that contribute to the current. Impact of variation in defect density at the interfaces of CdS/MoTe<sub>2</sub> and MoTe<sub>2</sub>/Cu<sub>2</sub>O are depicted in Fig. 7a and b, respectively. To run the simulations, the defect densities of both interfaces were adjusted between  $1 \times 10^{10}$  and  $1 \times 10^{21}$  cm<sup>-2</sup>. According to the study, as defect density increases from  $1 \times 10^{10}$  cm<sup>-2</sup> to  $1 \times 10^{21}$  cm<sup>-2</sup> at the CdS/MoTe<sub>2</sub> interface, PCE decreases from 32.38 to 23.46%, and at the MoTe<sub>2</sub>/Cu<sub>2</sub>O contact, PCE decreases from 32.38 to 26.91%. Moreover,  $J_{sc}$  and  $V_{oc}$  dropped as defect density increased. It is evident that increased defect density worsens cell output by increasing charge trapping [56]. To achieve a higher PV conversion efficiency, defects at the CdS/MoTe<sub>2</sub> and MoTe<sub>2</sub>/Cu<sub>2</sub>O interfaces were chosen at  $1 \times 10^{11}$  cm<sup>-2</sup>.

### 3.7 The influence of back surface recombination velocity and temperature on PV parameters

The surface recombination velocity (SRV) is equivalent to the lifetime of minority carriers within a bulk semiconductor. Figure 8a displays the impact of SRV variation from 10 to  $1 \times 10^9$  cm/s at the back contact on PV output parameters. Without Cu<sub>2</sub>O HTL,  $V_{oc}$  decreased from 1.06 to 0.9 V. After keeping a steady value till  $1 \times 10^3$ ,  $J_{sc}$  decreased from 35.12 to 34.51 mA/cm<sup>2</sup>. FF gained an initial increase, peaking at 87.82% for  $1 \times 10^3$  cm/s, then declined to the lowest 84.49% afterwards. PCE decreased with increasing SRV, ranging from 32.21 to 26.12%. The structure with HTL did not exhibit any change in PV parameters, keeping  $V_{oc} = 1.07$  V,  $J_{sc} = 35.13$  mA/cm<sup>2</sup>, FF = 86.32%, and PCE = 32.38%. The decrease of PV parameters in SC without HTL is attributed to the recombination loss at the back contact while the incorporation of Cu<sub>2</sub>O reduces back surface recombination. Comparable findings have been reported in earlier research [57, 58]. According to a recent report, a lower back SRV in a bulk semiconductor results in an optimal open circuit voltage as it is equivalent to the lifetime of minority carriers [59].

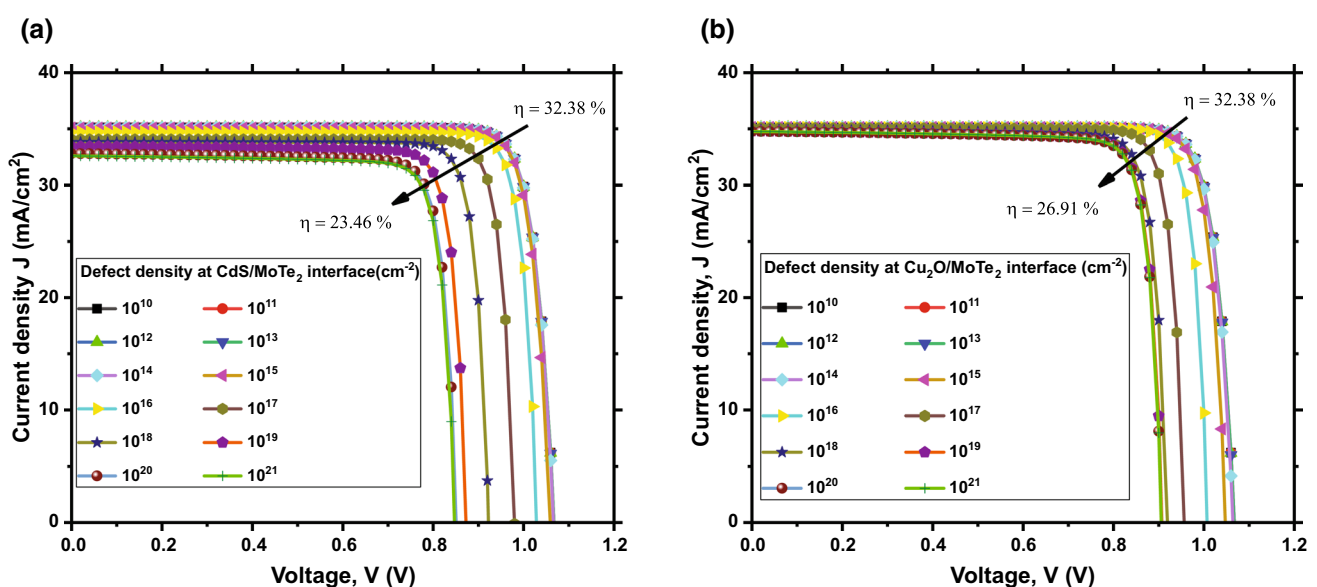
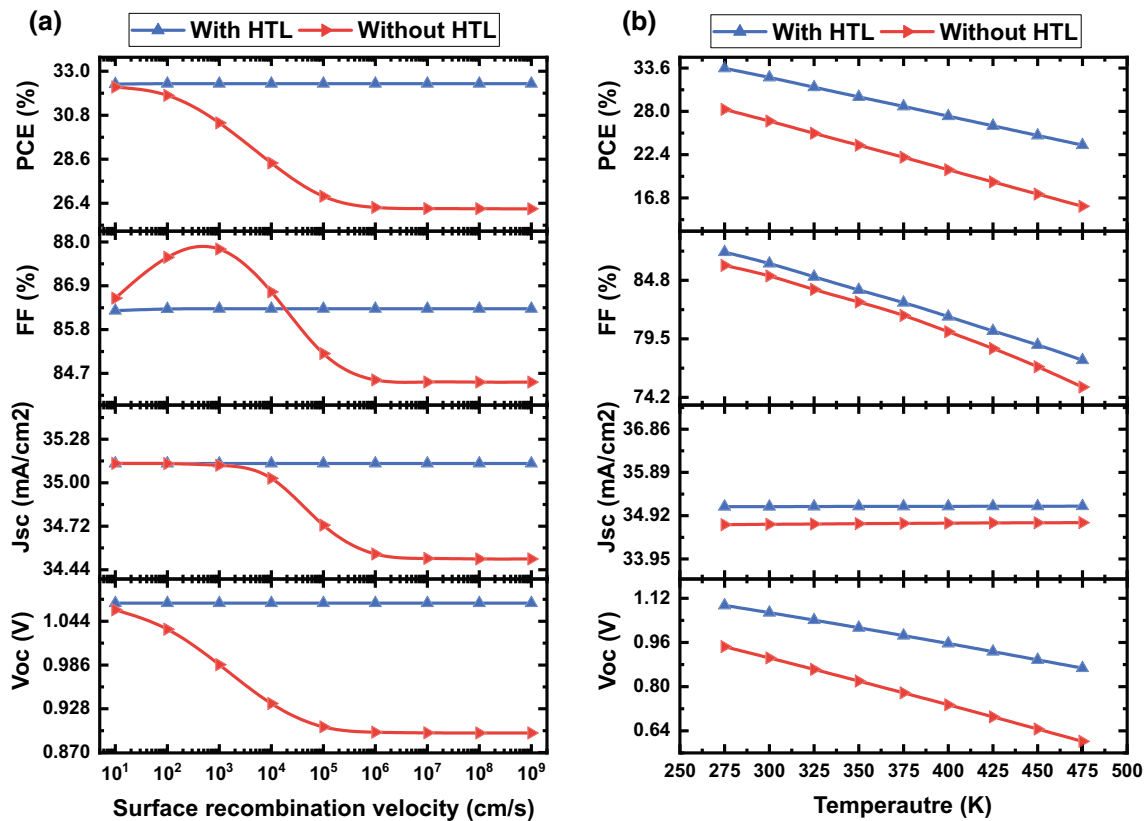


Fig. 7 The change of output parameters due to the variation of defect density at **a** CdS/MoTe<sub>2</sub> and **b** Cu<sub>2</sub>O/MoTe<sub>2</sub> interface



**Fig. 8** The variation of PV output parameters due to the change of **a** surface recombination velocity and **b** temperature

Investigations have been made on temperature effect of the SC structures. The operating temperature was varied from 275 to 475 K at intervals of 25 K under the fixed illumination condition of  $1000 \text{ W/m}^2$ . Figure 8b displays the PV parameters that were measured. Most of the semiconductor's parameters changed due to a decrease in bandgap caused by an increase in temperature. While the  $J_{sc}$  remained constant, it was observed that the other PV parameters declined linearly with increasing temperature. The production of most of the electron-hole pairs that contribute to this constant  $J_{sc}$  is facilitated by the increased energy of the dispositive electrons acquired at high temperatures. At 275 and 475 K, the proposed structure's PCE is numerically predicted to be 33.58 and 23.63%, respectively, while for the baseline structure, it is 28.25 and 15.72%. Previous studies have widely recognized the impact of operating temperatures on the degradation of PCE [60, 61]. According to the observation, the structure's optimum efficiency was attained at 275 K with PCE=33.58%, FF=87.36%,  $J_{sc}$  = 35.12 mA/cm<sup>2</sup>, and  $V_{oc}$  = 1.09 V.

### 3.8 Performance parameters variation due to series and shunt resistance

Two essential factors that have a substantial impact on the performance of solar cells are series and shunt resistance. The resistance that current encounters as it passes through the conductive contacts, intrinsic layer, and other layers of a solar cell is known as series resistance ( $R_s$ ). The voltage drop over high  $R_s$  might result in a large loss of power. The term shunt resistance ( $R_{sh}$ ) describes the parasitic resistance pathways present in solar cells that enables the current to pass through the active photoactive layer. High  $R_{sh}$  is preferred because it can improve solar cell open-circuit voltage and decrease leakage current.  $R_s$  is calculated as the total sum of the ohmic resistance of the cell and the contact resistance of the front, back, and contact between two layers. The  $R_{sh}$  results from a variety of different charge recombination processes, including leakage current across cell boundaries and surface deformation.

In this section, the electrical properties of the MoTe<sub>2</sub>-based solar cell with a Cu<sub>2</sub>O HTL are investigated in relation to the effects of  $R_s$  and  $R_{sh}$ . As shown in Fig. 9, the  $R_s$  and  $R_{sh}$  have been modified from 0 to  $4 \Omega\text{-cm}^2$  and  $1 \times 10^1$  to  $1 \times 10^7 \Omega\text{-cm}^2$ , respectively. Figure 9a shows the variation of  $V_{oc}$  with the change in  $R_s$  and  $R_{sh}$  values. As the  $R_s$  increased from 0 to  $4 \Omega\text{-cm}^2$ ,  $V_{oc}$  also increased gradually from 0.36 to 1.07 V for  $1 \times 10^1$  to  $1 \times 10^2 \Omega\text{-cm}^2$  of the  $R_{sh}$ . For the  $R_{sh}$  from  $1 \times 10^2$

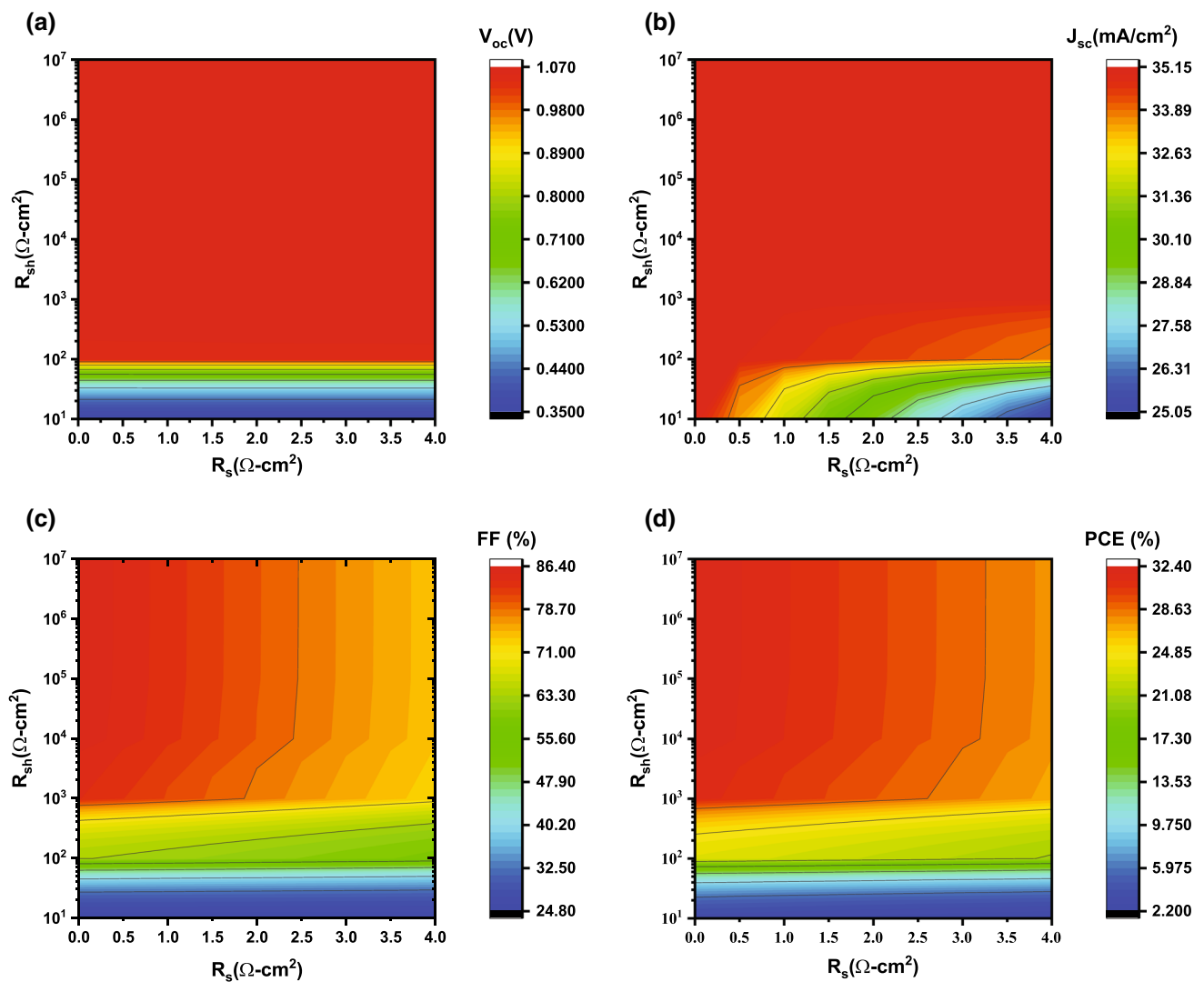


**Fig. 9** The variation of performance parameter due to series resistance and shunt resistance: **a**  $V_{oc}$ , **b**  $J_{sc}$ , **c** FF and **d** PCE

to  $1 \times 10^7 \Omega\text{-cm}^2$ ,  $V_{oc}$  (1.07 V) remained constant. The value of  $J_{sc}$  decreased from 35.11 to 25.05 mA/cm<sup>2</sup> as the  $R_s$  elevated from 0 to 4  $\Omega\text{-cm}^2$  with increasing  $R_{sh}$   $1 \times 10^1$  to  $1 \times 10^3 \Omega\text{-cm}^2$  as illustrated in Fig. 9b. The reason behind this decrease in  $J_{sc}$  with an increase in series resistance is that the series resistance affects the voltage drop across the cell, which in turn affects the current. As the series resistance increased, more voltage drop occurred across the resistance, leading to a decrease in the voltage across the cell and hence a decrease in  $J_{sc}$ . Looking at the plot, it is clear that increasing  $R_{sh}$  ( $> 1 \times 10^3 \Omega\text{-cm}^2$ ) has a negligible effect on  $J_{sc}$ , as the values remained almost constant (35.12 mA/cm<sup>2</sup>) across all shunt resistance values. The FF increased from 25 to 75% with the increment of  $R_{sh}$  up to  $1 \times 10^3 \Omega\text{-cm}^2$  with lower  $R_s$  ( $< 1 \Omega\text{-cm}^2$ ) as represented in Fig. 9c. For higher values of  $R_{sh}$  ( $> 1 \times 10^3 \Omega\text{-cm}^2$ ) in the lower  $R_s$  ( $< 1 \Omega\text{-cm}^2$ ) region, FF kept a maximum value of around 86%. From Fig. 9d, we can see that the PCE increased from 2.20 to 29% as the  $R_{sh}$  elevated up to  $1 \times 10^3 \Omega\text{-cm}^2$  with the decrease in  $R_s$  ( $< 1 \Omega\text{-cm}^2$ ). From  $R_{sh}$  value of  $1 \times 10^3 \Omega\text{-cm}^2$  and onward, PCE attained a constant maximum of around 32%. As the  $R_{sh}$  increased, the  $J_{sc}$  improved, leading to a higher PCE. On the other hand, as the  $R_s$  decreased, the FF increased, contributing to a higher PCE. Similar PV performances dependent on  $R_s$  and  $R_{sh}$  are also reported in previous studies [62, 63]. It is obvious that for the solar cell to function more effectively, the  $R_s$  should be low and the  $R_{sh}$  should be high.

### 3.9 Improvement of performance parameters and quantum efficiency

The illuminated J-V characteristics of the solar cell design with and without a  $\text{Cu}_2\text{O}$  hole transport layer are shown in Fig. 10a. The baseline structure Al/FTO/CdS/MoTe<sub>2</sub>/Ni attained  $V_{oc}$  of 0.90 V,  $J_{sc}$  of 34.73 mA/cm<sup>2</sup>, FF of 85.20%, and PCE of 26.74%, whereas the proposed structure Al/FTO/CdS/MoTe<sub>2</sub>/Cu<sub>2</sub>O/Ni attained PCE of 32.38%, with a  $V_{oc}$  of 1.07 V,  $J_{sc}$  of 35.12 mA/cm<sup>2</sup>, and FF of 86.32%. Between the MoTe<sub>2</sub> and back contact, the addition of the  $\text{Cu}_2\text{O}$  HTL layer significantly improved the PCE by about 5.6%. The improvement in performance parameters is attributable to a decrease in the dark current for surface recombination [48]. By lowering minority carrier recombination loss and producing a potent electric field that reflects photo-generated carriers in the direction of the front contact, the addition of a P<sup>+</sup>-type  $\text{Cu}_2\text{O}$  HTL between the absorber and rear contact layer improves efficiency. As a result, the performance parameters improve.

In Fig. 10b, it is shown how the proposed structure's external quantum efficiency (EQE) spectra with and without HTL change with wavelength. To study EQE, the wavelength was changed from 300 to 1100 nm under the 1.5AM solar illumination. After the addition of  $\text{Cu}_2\text{O}$  layer, the proposed MoTe<sub>2</sub>-based heterojunction solar cells' quantum efficiency increased at wavelengths  $\lambda > 750$  nm. The proposed solar cell with  $\text{Cu}_2\text{O}$  has been shown to have high EQE when compared to the baseline structure. By generating strong back surface electric fields at the  $\text{Cu}_2\text{O}/\text{MoTe}_2$  interface and enhancing the absorption edge at the higher wavelength range, the  $\text{Cu}_2\text{O}$  HTL layer's insertion into the proposed SC structure reduces photogenerated carrier recombination and helps to maximize the overall performance parameters of the SC [51].

The development of MoTe<sub>2</sub>-based SC configurations examined by various research groups is listed in Table 3. According to the earlier stated works, the PCE of MoTe<sub>2</sub>-based SCs improved from 25.06 to 29.13%. One of the noteworthy causes of this improvement is the decrease in carrier recombination and enhanced band alignment at the HTL/absorber and absorber/ETL. The highly doped p<sup>+</sup>- $\text{Cu}_2\text{O}$  HTL for MoTe<sub>2</sub> absorber can generate the ideal band alignment and electric field at the HTL/absorber interface to restrict minority carrier flow toward the back metallic electrode, reducing recombination loss and improving  $V_{oc}$ . By using earth-abundant and inexpensive materials like MoTe<sub>2</sub> and  $\text{Cu}_2\text{O}$ , our numerical simulation was able to improve  $V_{oc}$ ,  $J_{sc}$ , and PCE in comparison to previously reported values as represented in table-3, potentially lowering the cost of fabricating SCs.

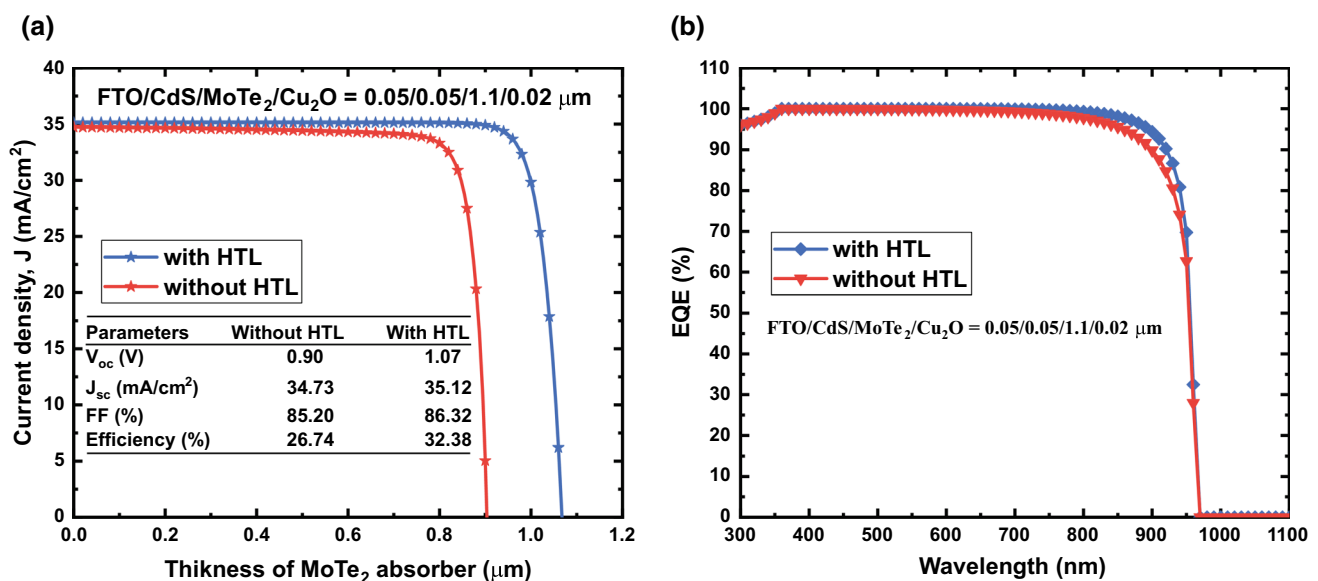


Fig. 10 **a** J-V curve and **b** EQE of proposed and reference MoTe<sub>2</sub> solar cell

**Table 3** Performance comparison with previously published reports on TMDC-based SCs.

Structure	Study type	Absorber layer thickness	$J_{sc}$ (mA/cm <sup>2</sup> )	$V_{oc}$ (V)	FF (%)	PCE (%)	References
ITO/MoS <sub>2</sub> /Au	Experiment	0.22	5.37	0.597	55	1.8	[64]
n-MoS <sub>2</sub> /p-Si	Experiment	5.0	22.36	0.41	57.0	5.23	[65]
ITO/TiO <sub>2</sub> /MoS <sub>2</sub> /P3HT/Au	Experiment	2.0	4.7	0.56	-	1.3	[66]
ZnO/ZnS/MoSe <sub>2</sub>	Theory	0.4	22.19	0.795	-	17.51	[11]
SnO <sub>2</sub> /Zn <sub>2</sub> SnO <sub>4</sub> /CdS/MoTe <sub>2</sub> /ZnTe	Theory	1.0	27.91	1.07	84.2	25.16	[21]
SnO <sub>2</sub> /Zn <sub>2</sub> SnO <sub>4</sub> /CdS/MoTe <sub>2</sub> /As <sub>2</sub> Te <sub>3</sub>	Theory	1.0	27.79	1.07	84.2	25.06	[22]
SnO <sub>2</sub> /Zn <sub>2</sub> SnO <sub>4</sub> /CdS/MoTe <sub>2</sub> /CZT	Theory	0.8	27.85	1.07	84.1	25.11	[12]
SnO <sub>2</sub> /Zn <sub>2</sub> SnO <sub>4</sub> /CdS/MoTe <sub>2</sub> /In <sub>2</sub> Te <sub>3</sub>	Theory	1.0	27.90	1.07	84.2	25.17	[67]
FTO/CdS/MoTe <sub>2</sub> /Cu <sub>2</sub> Te	Theory	0.5	38.71	0.88	85.26	29.13	[15]
FTO/CdS/MoTe <sub>2</sub>	Theory	1.1	34.73	0.90	85.20	26.74	Baseline structure
FTO/CdS/MoTe <sub>2</sub> /Cu <sub>2</sub> O	Theory	1.1	35.12	1.07	86.32	32.38	Proposed structure

## 4 Conclusion

In this study, the Al/FTO/CdS/MoTe<sub>2</sub>/Cu<sub>2</sub>O/Ni structured TFSC was methodically modeled and simulated via SCAPS-1D. For the baseline structure, a similar configuration without a Cu<sub>2</sub>O hole transport layer was selected. To achieve the best possible PCE for the suggested structure, a MoTe<sub>2</sub> absorption layer with a thickness of 1.1 μm, doping density of  $5 \times 10^{15} \text{ cm}^{-3}$ , Cu<sub>2</sub>O HTL with a thickness of 0.02 μm, doping density of  $1 \times 10^{18} \text{ cm}^{-3}$  and a CdS ETL of 0.05 μm thickness have been selected. Our simulation investigations demonstrate the effects of several parameters, including thickness, doping concentration, interface defects, HTL electron affinity, contact metal work function, surface recombination, parasitic resistances ( $R_s$  and  $R_{sh}$ ), and operating temperature. With a  $V_{oc}$  of 1.07 V, a  $J_{sc}$  of 35.12 mA/cm<sup>2</sup>, and an FF of 86.32%, the proposed structure achieved PCE of 32.38%. According to these findings, the Al/FTO/CdS/MoTe<sub>2</sub>/Cu<sub>2</sub>O/Ni structure is a good contender for high-efficiency solar cells. This research work offers instructions for producing a highly effective MoTe<sub>2</sub>-based PV cell. The results provide valuable insights for future developments in the field of heterojunction TMDC devices and their potential for efficient solar energy conversion.

**Acknowledgements** The authors are very grateful to Dr. Marc Burgelman of the University of Gent in Belgium for providing the SCAPS-1D simulation program.

**Author contributions** NR conceived the idea, performed data collection, conducted simulations, and contributed to writing the manuscript. Md. DH provided supervision, performed editing, and contributed to writing the manuscript. Md. FR performed validation, review, and editing. Md. MI provided supervision and contributed to editing the manuscript. Most. ANJ and ARR assisted with the simulations. Most. AA and Md. FI assisted with generated data processing and figure preparation.

**Funding** The authors state that they did not receive any money, grants, or other financial support for the manuscript's preparation.

**Data availability** The data and materials supporting the findings will be made available upon reasonable request to the corresponding author.

## Declarations

**Ethics approval and consent to participate** Not applicable.

**Competing interests** The authors declare no competing interests.

**Open Access** This article is licensed under a Creative Commons Attribution 4.0 International License, which permits use, sharing, adaptation, distribution and reproduction in any medium or format, as long as you give appropriate credit to the original author(s) and the source, provide a link to the Creative Commons licence, and indicate if changes were made. The images or other third party material in this article are included in the article's Creative Commons licence, unless indicated otherwise in a credit line to the material. If material is not included in the article's Creative Commons licence and your intended use is not permitted by statutory regulation or exceeds the permitted use, you will need to obtain permission directly from the copyright holder. To view a copy of this licence, visit <http://creativecommons.org/licenses/by/4.0/>.

## References

1. ISE, P.R.I.F.O.R.S. E.S.: Photovoltaics Report. 2023.
2. Green M, Dunlop E, Hohl-Ebinger J, Yoshita M, Kopidakis N, Hao X. Solar cell efficiency tables (version 57). *Prog Photovoltaics Res Appl.* 2021;29:3–15. <https://doi.org/10.1002/pip.3371>.
3. Atowar Rahman M. Enhancing the photovoltaic performance of Cd-free Cu<sub>2</sub>ZnSnS<sub>4</sub> heterojunction solar cells using SnS HTL and TiO<sub>2</sub> ETL. *Sol Energy.* 2021;215:64–76. <https://doi.org/10.1016/j.solener.2020.12.020>.
4. Katagiri H, Jimbo K, Maw WS, Oishi K, Yamazaki M, Araki H, Takeuchi A. Development of CZTS-based thin film solar cells. *Thin Solid Films.* 2009;517:2455–60. <https://doi.org/10.1016/j.tsf.2008.11.002>.
5. Candelise C, Winkler M, Gross R. Implications for CdTe and CIGS technologies production costs of indium and tellurium scarcity. *Prog Photovoltaics Res Appl.* 2012;20:816–31. <https://doi.org/10.1002/pip.2216>.
6. Tao M. Roadblocks to Terawatt Solar Photovoltaics. *SpringerBriefs in Applied Sciences and Technology.* 61–79. Springer Verlag 2014.
7. Li H, Huang J-K, Shi Y, Li L-J. Toward the growth of high mobility 2D transition metal dichalcogenide semiconductors. *Adv Mater Interfaces.* 2019;6:1900220. <https://doi.org/10.1002/admi.201900220>.
8. Nassiri Nazif K, Daus A, Hong J, Lee N, Vaziri S, Kumar A, Nitta F, Chen ME, Kananian S, Islam R. Others: high-specific-power flexible transition metal dichalcogenide solar cells. *Nat Commun.* 2021;12:7034. <https://doi.org/10.1038/s41467-021-27195-7>.
9. Velusamy DB, Kim RH, Cha S, Huh J, Khazaeinezhad R, Kassani SH, Song G, Cho SM, Cho SH, Hwang I. Others: flexible transition metal dichalcogenide nanosheets for band-selective photodetection. *Nat Commun.* 2015;6:8063. <https://doi.org/10.1038/ncomms9063>.
10. Chhowalla M, Shin HS, Eda G, Li LJ, Loh KP, Zhang H. The chemistry of two-dimensional layered transition metal dichalcogenide nanosheets. *Nat Chem.* 2013;5:263–75. <https://doi.org/10.1038/nchem.1589>.
11. Zaidi B, Shekhar C, Hadjoudja B, Gagui S, Chouial B. Optimization of highly efficient monolayer MoSe<sub>2</sub> based solar cells. *Acta Phys Pol A.* 2019;136:495–7. <https://doi.org/10.12693/APhysPolA.136.495>.
12. Dey MM, Dey MM, Das NK, Gupta AKS, Sen, Matin MA, Amin N. Performance improvement of highly stable molybdenum telluride solar cells with CZT BSF. *ECCE 2017 - International Conference on Electrical, Computer and Communication Engineering.* 941–945. 2017; <https://doi.org/10.1109/ECACE.2017.7913038>.
13. Jaegermann W, Tributsch H. Interfacial properties of semiconducting transition metal chalcogenides. *Prog Surf Sci.* 1988;29:1–167. [https://doi.org/10.1016/0079-6816\(88\)90015-9](https://doi.org/10.1016/0079-6816(88)90015-9).
14. Pradhan NR, Rhodes D, Feng S, Xin Y, Memaran S, Moon B-H, Terrones H, Terrones M, Balicas L. Field-effect transistors based on few-layered  $\alpha\text{-}\text{MoTe}_2$ . *ACS Nano.* 2014;8:5911–20. <https://doi.org/10.1021/nn501013c>.
15. Faisal S, Rahman SI, Ahmed S, Dhruvo TI. Numerical analysis of MoTe<sub>2</sub> thin film solar cell with Cu<sub>2</sub>Te BSF layer. *IEEE Region 10 Annual International Conference, Proceedings/TENCON.* 2017-Decem, 2342–2346 2017; <https://doi.org/10.1109/TENCON.2017.8228252>.
16. Frindt RF. The optical properties of single crystals of WSe<sub>2</sub> and MoTe<sub>2</sub>. *J Phys Chem Solids.* 1963;24:1107–8. [https://doi.org/10.1016/0022-3697\(63\)90024-6](https://doi.org/10.1016/0022-3697(63)90024-6).
17. Pandey K, Patel AK, Mishra R. Numerical study on performance enhancement of CZTSSe solar cells with Cu<sub>2</sub>O and MoTe<sub>2</sub> as hole transport layer. *J Comput Electron.* 2022;21:895–904. <https://doi.org/10.1007/s10825-022-01900-1>.
18. Hussain S, Patil SA, Vikraman D, Rabani I, Arbab AA, Jeong SH, Kim HS, Choi H, Jung J. Enhanced electrocatalytic properties in MoS<sub>2</sub>/MoTe<sub>2</sub> hybrid heterostructures for dye-sensitized solar cells. *Appl Surf Sci.* 2020;504:144401. <https://doi.org/10.1016/j.apsusc.2019.144401>.
19. Vikraman D, Hussain S, Jaffery A, Liu SH, Karuppasamy H, Sanmugam K, Jung A, Kim J. Tuning the layered thickness of MoTe<sub>2</sub> thin film for dye-sensitized solar cells, UV and visible spectrum photodetectors, and hydrogen evolution reaction. *Solar RRL.* 2022. <https://doi.org/10.1002/solr.202200610>.
20. Hussain S, Patil SA, Vikraman D, Mengal N, Liu H, Song W, An K-SS, Jeong SH, Kim H-SS, Jung J. Large area growth of MoTe<sub>2</sub> films as high performance counter electrodes for dye-sensitized solar cells. *Sci Rep.* 2018;8:1–9. <https://doi.org/10.1038/s41598-017-18067-6>.
21. Dey MM, Dey MM, Matin MA, Amin N. Enhancement the performance of Molybdenum Telluride solar cells with Zinc Telluride BSF. In: 2016 International Conference on Innovations in Science, Engineering and Technology (ICSET). pp. 1–5. 2016.
22. Dey MM, Dey MM, Matin MA, Amin N. Design of highly stable and efficient molybdenum telluride PV cells with arsenic telluride BSF. 2016 3rd International Conference on Electrical Engineering and Information and Communication Technology, iCEEICT 2016. 4–8. 2017. <https://doi.org/10.1109/CEEICT.2016.7873153>.
23. Rahman MA. Design and simulation of a high-performance Cd-free Cu<sub>2</sub>SnSe<sub>3</sub> solar cells with SnS electron-blocking hole transport layer and TiO<sub>2</sub> electron transport layer by SCAPS-1D. *SN Appl Sci.* 2021;3:253. <https://doi.org/10.1007/s42452-021-04267-3>.
24. MostR Sultana, Islam B, Ahmed SR, Al. Modeling and performance analysis of highly efficient copper indium gallium selenide solar cell with Cu<sub>2</sub>O hole transport layer using solar cell capacitance simulator in one dimension. *Physica status solidi.* 2022;219:2100512. <https://doi.org/10.1002/pssa.202100512>.
25. Baig F, Khattak YH, Shuja A, Riaz K, Soucase BM. Performance investigation of Sb<sub>2</sub>Se<sub>3</sub> based solar cell by device optimization, band offset engineering and hole transport layer in SCAPS-1D. *Curr Appl Phys.* 2020;20:973–81. <https://doi.org/10.1016/j.cap.2020.06.005>.
26. Hosen A, Ahmed SR, Al. Performance analysis of SnS solar cell with a hole transport layer based on experimentally extracted device parameters. *J Alloys Compd.* 2022;909:164823. <https://doi.org/10.1016/j.jallcom.2022.164823>.
27. Kumar A, Ranjan P. Computational analysis of chalcogenides as an inorganic hole transport layer in perovskite solar cells. *Opt Quantum Electron.* 2021;53:1–15. <https://doi.org/10.1007/s11082-021-03186-2>.
28. Hilal M, Han JI. Interface engineering of G-PEDOT: PSS hole transport layer via interlayer chemical functionalization for enhanced efficiency of large-area hybrid solar cells and their charge transport investigation. *Sol Energy.* 2018;174:743–56. <https://doi.org/10.1016/j.solener.2018.09.031>.
29. Yaghoobi Nia N, Bonomo M, Zendehdel M, Lamanna E, Desoky MMH, Paci B, Zurlo F, Generosi A, Barolo C, Viscardi G, Quagliotto P, Di Carlo A. Impact of P3HT regioregularity and molecular weight on the efficiency and stability of perovskite solar cells. *ACS Sustain Chem Eng.* 2021;9:5061–73. <https://doi.org/10.1021/acssuschemeng.0c09015>.

30. Han J, Tu Y, Liu Z, Liu X, Ye H, Tang Z, Shi T, Liao G. Efficient and stable inverted planar perovskite solar cells using dopant-free CuPc as hole transport layer. *Electrochim Acta*. 2018;273:273–81. <https://doi.org/10.1016/j.electacta.2018.04.055>.
31. Verma UK, Kumar B. Charge transport in quantum dot organic solar cells with Si quantum dots sandwiched between poly(3-hexylthiophene) (P3HT) absorber and bathocuproine (BCP) transport layers. *J Appl Phys*. 2017;122:153104. <https://doi.org/10.1063/1.4996845>.
32. Brandt J, Fröhlich D, Sandfort C, Bayer M, Stolz H, Naka N. Ultranarrow optical absorption and two-phonon excitation spectroscopy of Cu<sub>2</sub>O paraexcitons in a high magnetic field. *Phys Rev Lett*. 2007;99:217403. <https://doi.org/10.1103/PhysRevLett.99.217403>.
33. Chatterjee S, Pal AJ. Introducing Cu<sub>2</sub>O thin films as a hole-transport layer in efficient planar perovskite solar cell structures. *J Phys Chem C*. 2016;120:1428–37. <https://doi.org/10.1021/acs.jpcc.5b11540>.
34. Lee YS, Heo J, Winkler MT, Siah SC, Kim SB, Gordon RG, Buonassisi T. Nitrogen-doped cuprous oxide as a p-type hole-transporting layer in thin-film solar cells. *J Mater Chem A Mater*. 2013;1:15416–22. <https://doi.org/10.1039/c3ta13208k>.
35. ABENA AMN, NGOUPO AT, ABEGA FXA, NDJAKA JMB. Numerical investigation of solar cells based on hybrid organic cation perovskite with inorganic HTL via SCAPS-1D. *Chin J Phys*. 2022;76:94–109. <https://doi.org/10.1016/j.cjph.2021.12.024>.
36. Abdelkadir AA, Oublal E, Sahal M, Gibaud A, Ait Abdelkadir A, Oublal E, Sahal M, Gibaud A. Numerical simulation and optimization of n-Al-ZnO/n-CdS/p-CZTSe/p-NiO (HTL)/Mo solar cell system using SCAPS-1D. *Results in Optics*. 2022;8.
37. Simya OK, Mahaboobbatcha A, Balachander K. Compositional grading of CZTSSe alloy using exponential and uniform grading laws in SCAPS-1D simulation. *Superlattices Microstruct*. 2016;92:285–93. <https://doi.org/10.1016/j.spmi.2016.02.019>.
38. Burgelman M, Nollet P, Degraeve S. Modelling polycrystalline semiconductor solar cells. *Thin Solid Films*. 2000;361:527–32. [https://doi.org/10.1016/S0040-6090\(99\)00825-1](https://doi.org/10.1016/S0040-6090(99)00825-1).
39. Gan Y, Bi X, Liu Y, Qin B, Li Q, Jiang Q, Mo P, Xueguang B, Yucheng L, Binyi Q, Qingliu L, Qubo J, Pei M. Numerical investigation energy conversion performance of tin-based perovskite solar cells using cell capacitance simulator. *Energies (Basel)*. 2020;13:5907. <https://doi.org/10.3390/en13225907>.
40. Haque MD, Ali MH, Rahman MF, Islam AZMT. Numerical analysis for the efficiency enhancement of MoS<sub>2</sub> solar cell: a simulation approach by SCAP-1D. *Opt mater*. 2022;131:112678. <https://doi.org/10.1016/j.optmat.2022.112678>.
41. Hossain MK, Arnab AA, Das RC, Hossain KM, Rubel MHK, Rahman MF, Bencherif H, Emeter ME, Mohammed MKA, Pandey R. Combined DFT, SCAPS-1D, and wxAMPS frameworks for design optimization of efficient cs 2 BiAgI 6-based perovskite solar cells with different charge transport layers. *RSC Adv*. 2022;12:35002–25. <https://doi.org/10.1039/D2RA06734J>.
42. Patel AK, Rao PK, Mishra R, Soni SK. Numerical study of a highperformance thin film CIGS solar cell with a-Si and MoTe<sub>2</sub> hole transport layer. *Optik (Stuttg)*. 2021;243:167498. <https://doi.org/10.1016/j.ijleo.2021.167498>.
43. Meng Y, Magruder BR, Hillhouse HW. On interface recombination, series resistance, and absorber diffusion length in BiI<sub>3</sub> solar cells. *J Appl Phys*. 2021. <https://doi.org/10.1063/5.0034776>.
44. Chen L, Fang C, Liu W. Influence of absorption layer thickness on the performance of CIGS solar cells. *IOP Conf Ser Earth Environ Sci*. 2020. <https://doi.org/10.1088/1755-1315/440/3/032051>.
45. Aydin B, Duman Ç. Optimization of electrode, interlayer and absorber layers of a Gr/ReS<sub>2</sub>/PSi/p-cSi photovoltaic solar cell with SCAPS. *J Electron Mater*. 2023;52:4809–21. <https://doi.org/10.1007/s11664-023-10415-9>.
46. Moustafa M, Zoubi A, Yasin T. Numerical analysis of the role of p-MoSe<sub>2</sub> interfacial layer in CZTSe thin-film solar cells using SCAPS simulation. *Optik (Stuttg)*. 2021;247:167885. <https://doi.org/10.1016/j.ijleo.2021.167885>.
47. Ball JM, Petrozza A. Defects in perovskite-halides and their effects in solar cells. *Nat Energy*. 2016;1:1–13. <https://doi.org/10.1038/NENERGY.2016.149>.
48. Moustafa M, Alzoubi T. Numerical study of CdTe solar cells with p-MoTe<sub>2</sub> TMDC as an interfacial layer using SCAPS. *Mod Phys Lett B*. 2018;32:1–11. <https://doi.org/10.1142/S021798491850269X>.
49. Kutwade VV, Gattu KP, Sonawane ME, Tonpe DA, Mohammed IMS, Sharma R. Theoretical modeling and optimization: Cd-free CTS/Zn (o, S)/ZnO thin film solar cell. *Mater Today Commun*. 2021;29:102972. <https://doi.org/10.1016/j.mtcomm.2021.102972>.
50. Hasan Ali M, Saiful Islam ATM, Haque MD, Ferdous Rahman M, Khalid Hossain M, Sultana N, Islam T. Numerical analysis of FeSi<sub>2</sub> based solar cell with PEDOT:PSS hole transport layer. *Mater Today Commun*. 2023;34:105387. <https://doi.org/10.1016/j.mtcomm.2023.105387>.
51. Liyanage GK, Phillips AB, Alfadhili FK, Ellingson RJ, Heben MJ. The role of back buffer layers and Absorber Properties for > 25% efficient CdTe solar cells. *ACS Appl Energy Mater*. 2019;2:5419–26. <https://doi.org/10.1021/acs.aem.9b00367>.
52. Liyanage GK, Phillips AB, Heben MJ. Role of band alignment at the transparent front contact/emitter interface in the performance of wide bandgap thin film solar cells. *APL Mater*. 2018;6:101104. <https://doi.org/10.1063/1.5051537>.
53. Sajid S, Alzahmi S, Salem I, Ben, Obaidat IM. Guidelines for fabricating highly efficient perovskite solar cells with Cu<sub>2</sub>O as the hole transport material. *Nanomaterials*. 2022;12:3315. <https://doi.org/10.3390/nano12193315>.
54. Khatoun S, Yadav SK, Singh J, Singh RB. Design of a CH<sub>3</sub>NH<sub>3</sub>PbI<sub>3</sub>/CsPbI<sub>3</sub>-based bilayer solar cell using device simulation. *Heliyon*. 2022;8:e09941. <https://doi.org/10.1016/j.heliyon.2022.e09941>.
55. Hölzl J, Schulte FK. Work function of metals. 1–150 1979. <https://doi.org/10.1007/bfb0048919>.
56. Lokhande AC, Babar PT, Karade VC, Gang MG, Lokhande VC, Lokhande CD, Kim JH. The versatility of copper tin sulfide. *J Mater Chem A Mater*. 2019;7:17118–82. <https://doi.org/10.1039/C9TA00867E>.
57. Amin N, Sopian K, Konagai M. Numerical modeling of CdS/CdTe and CdS/CdTe/ZnTe solar cells as a function of CdTe thickness. *Sol Energy Mater Sol Cells*. 2007;91:1202–8. <https://doi.org/10.1016/j.solmat.2007.04.006>.
58. Ma Y, Dai Y, Guo M, Niu C, Lu J, Huang B. Electronic and magnetic properties of perfect, vacancy-doped, and nonmetal adsorbed MoSe<sub>2</sub>, MoTe<sub>2</sub> and WS<sub>2</sub> monolayers. *Phys Chem Chem Phys*. 2011;13:15546–53. <https://doi.org/10.1039/c1cp21159e>.
59. Kumar A, Ranjan P. Defects signature in VOC characterization of thin-film solar cells. *Sol Energy*. 2021;220:35–42. <https://doi.org/10.1016/j.solener.2021.03.017>.
60. Gautam S, Patel AK, Mishra R, Mishra O. Performance analysis of WSe<sub>2</sub> solar cell with Cu<sub>2</sub>O hole transport layer by optimization of electrical and optical properties. *J Comput Electron*. 2022;21:1373–85. <https://doi.org/10.1007/s10825-022-01941-6>.
61. Haque MD, Ali MH, Islam AZMT. Efficiency enhancement of WSe<sub>2</sub> heterojunction solar cell with CuSCN as a hole transport layer: a numerical simulation approach. *Sol Energy*. 2021;230:528–37. <https://doi.org/10.1016/j.solener.2021.10.054>.



62. Hosen A, Mian MS, Ahmed SR, Al. Simulating the performance of a highly efficient CuBi2O4-based thin-film solar cell. *SN Appl Sci.* 2021;3:1–13. <https://doi.org/10.1007/s42452-021-04554-z>.
63. Khatun MM, Sunny A, Ahmed SR, Al. Numerical investigation on performance improvement of WS2 thin-film solar cell with copper iodide as hole transport layer. *Sol Energy.* 2021;224:956–65. <https://doi.org/10.1016/j.solener.2021.06.062>.
64. Shanmugam M, Durcan CA, Yu B. Layered semiconductor molybdenum disulfide nanomembrane based Schottky-barrier solar cells. *Nanoscale.* 2012;4:7399. <https://doi.org/10.1039/c2nr32394j>.
65. Tsai ML, Su SH, Chang JK, Tsai DS, Chen CH, Wu CI, Li LJ, Chen LJ, He JH. Monolayer MoS2 heterojunction solar cells. *ACS Nano.* 2014;8:8317–22. <https://doi.org/10.1021/nn502776h>.
66. Shanmugam M, Bansal T, Durcan CA, Yu B. Molybdenum disulphide/titanium dioxide nanocomposite-poly 3-hexylthiophene bulk heterojunction solar cell. *Appl Phys Lett.* 2012;100:1–5. <https://doi.org/10.1063/1.3703602>.
67. Dey MM, Dey MM, Matin MA, Amin N. High performance and stable molybdenum telluride PV cells with Indium Telluride BSF. *ICDRET 2016–4th International Conference on the Developments in Renewable Energy Technology.* 4–7 2016.

**Publisher's Note** Springer Nature remains neutral with regard to jurisdictional claims in published maps and institutional affiliations.